CONTROL TECHNOLOGY READINESS FOR SPACEBORNE OPTICAL INTERFEROMETER MISSIONS *

Gregory W. NEAT, Alex ABRAMOVICI, James W. MELODY,
Robert J. CALVET, Noble M. NERHEIM, and John F. O'BRIEN

Jet Propulsion Laboratory
California Institute of Technology
Pasadena, CA 91009

Abstract

This paper describes the Micro-Precision Interferometer (MPI) testbed and its major achievements to date related to mitigating risk for future spaceborne optical interferometer missions. The MPI testbed is a ground-based hardware model of a future spaceborne interferometer. The three primary objectives of the testbed are to: (1) demonstrate the 10 nm positional stability requirement in the ambient lab disturbance environment, (2) predict whether the 10 nm positional stability requirement can be achieved in the anticipated on-orbit disturbance environment, and (3) validate integrated modeling tools that will ultimately be used to design the actual space missions. This paper describes both the hardware testbed and the testbed simulation model in their present configurations. This paper presents results showing closed loop positional stabilities at or below the 10 nm requirement for both the ambient and on-orbit disturbance environments. In addition, the paper presents model validation results in which the MPI model predictions are within a factor of two of the actual MPI measurements. These encouraging ground-based results suggest that the control technologies and modeling tools are well on the way to reaching the maturity needed to understand and solve the on-orbit control challenges for spaceborne optical interfometers.

1 BACKGROUND

1.1 Introduction

A primary NASA objective is to discover and characterize planetary systems around other stars. Indirect planet detection methods exploit the fact that the gravitational pull of the revolving planet (s) cause the central star to "wobble" as viewed from many parsecs [1]. The larger the planet, the larger the induced "wobble". To discover earth-like planets around other stars requires micro-arcsecond astrometric measurement accuracy [1]. Spaceborne optical interferometers provide the only feasible method to significantly improve astrometric accuracy of current astronomical telescopes such as the Hubble Space Telescope (HST).

● Presented at The Space Microdynamics and Accurate Control Symposium, Toulouse, France, May, 1997

This partial aperture approach offers a number of important advantages over the traditional full aperture approach including: control of systematic errors, lower mass without loss of performance, and improved performance for a given amount of collecting area. However, this approach must emulate the optical surface quality of its full aperture counterpart, with many optical elements distributed across a light weight flexible structure. Achieving these nanometer-level positional stability requirements in the on-orbit disturbance environment is the primary control design challenge for this mission class.

This paper presents an overview of a ground-based model of a future space-based interferometer which is designed in part to answer questions about on-orbit vibration attenuation performance. The paper describes the testbed, the testbed's primary thrust areas and latest results from these areas.

1.2 Optical Interferometry

Optical interferometers use two (or more) smaller telescopes, as opposed to a traditional single large telescope, to collect light from a single target star. The light from these telescopes, or sub-apertures, is combined, creating an interference fringe pattern. By measuring the fringe pattern for different interferometer orientations, an aperture diameter equal to the separation of the two sub-apertures (the interferometer baseline) is synthesized. This allows for more accurate stellar measurements, since astrometric accuracy varies inversely to aperture diameter. Specifically for interferometers, astrometric accuracy is proportional to the ratio of stabilized fringe position to baseline length (for a given number of photons) [2]. Significant improvement in astrometric accuracy over existing full-aperture systems requires stabilization and measurement of stellar fringe position down to the 10 nanometer (RMS) level over baseline lengths of 7-20m [2], [3], [4].

In ground-based applications of this approach such as the Mark III interferometer located on Mt. Wilson [5], or the Palomar Testbed Interferometer on Mt. Palomar [6], atmospheric turbulence limits the instrument's ability to stabilize fringe position. For faint targets which require integration periods longer than the atmospheric coherence period, fringe position cannot be measured and therefore cannot be stabilized. In contrast, for the space-based incarnation of this approach, the primary challenge in stabilizing fringe position is rejecting onboard machinery disturbances.

The Stellar Interferometer Mission (SIM) is a mission concept for a first-generation space interferometer with astrometric and imaging goals [2], [3], [4]. The mission plan includes a 900 km Sun-synchronous orbit with an orbit period of 103 min. SIM uses three colinear Michelson interferometers to perform *μarcsec level* astrometric measurements and milliarcsec-level imaging of the heavens. Unlike the ground-based interferometers which are bolted to bedrock, the hardware for the space-based instrument is distributed across a 10m light weight truss structure.

1.3 Enabling Control Technology

For the last several years, the Jet Propulsion Laboratory (JPL) Interferometer Technology Program (ITP) has been developing new technologies required by future spaceborne inter-

ferometer missions [7]. The technology program contains two development efforts dictated by the primary technology needs: achieving nanometer positional stabilities of specific optical elements in the on-orbit disturbance environment and performing pico-meter relative metrology measurements. This paper focuses on the former. Details on the progress made in the metrology area can be found in references [8] and [9].

The Interferometer Technology Program evolved from a system design for the Focus Mission Interferometer (FMI): a space-based, 30 m baseline, partial aperture telescope concept [10]. Using analytical models of the spacecraft and disturbance environment, this effort predicted 1 micron (RMS) on-orbit fringe position motion in the unattenuated spacecraft environment. This fringe motion is a factor of 100 above the desired level of 10 nm (RMS). This discrepancy inspired the layered vibration attenuation strategy. Figure 1 presents the fundamental approach in terms of the three vibration attenuation layers: vibration isolation, structural quieting, and active optics. The strategy is to isolate vibrating machinery at the point of attachment, to damp specific undesirable structural modes that limit optical control system bandwidths, and to actively control specific optical elements to achieve the desired optical performance.

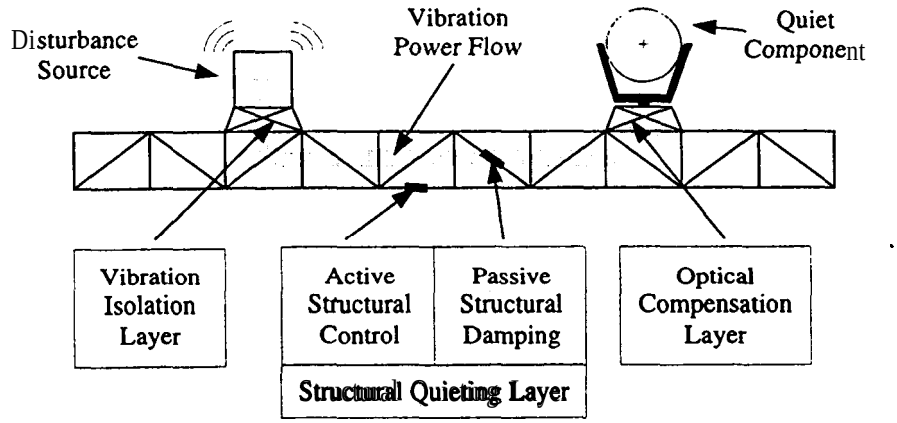

Figure 1: Interferometer Technology Program's layered control approach.

A 'number of analytical and hardware tools have been developed to understand the vibration attenuation challenge posed by spaceborne interferometers. These tools have been used to evaluate the layered control technology.

The complex opto-mechanical nature of the FMI analysis dictated the need for an integrated controls-structures-optics modeling environment. The Integrated Modeling of Optical Systems (IMOS) [12] software package was developed to meet this need. IMOS enables the integration of controls, structures, and optics models necessary for end-to-end disturbance analysis of spaceborne interferometers. Evaluations of the layered control technology applied to different interferometry missions, using IMOS, support the results from the original FMI analysis: that some form of vibration attenuation technology is essential to meet mission science goals [13], [14], [15].

The ITP Phase B testbed provided the first hardware validation of the layered control technology. The goal for this 3 m cantilevered truss structure was to stabilize an optical

pathlength to the nanometer-level in the presence of a single-axis shaker input disturbance using a single-axis vibration isolation stage, a number of active and passive structural damp ing struts, and an active optical delay line. The results indicated a factor of 5000 attenuation from input disturbance to output optical pathlength, with output variations on the order of 5 nm (RMS) [16]. The next logical step was to validate the layered control approach in hardware on a complete end-to-end instrument. This led to the design and assembly of the Micro-Precision Interferometer (MPI) testbed.

1.4 MPI Overview

Figure 2 shows a bird's eye view of the MPI testbed. Located at JPL, the MPI testbed is a ground-based, suspended hardware model of a future space-based interferometer. The testbed is approximately a full-scale model of SIM and contains all the necessary subsystems to assess the disturbance rejection technology status. These subsystems include: a 7m x 7m x 6.5m softly suspended truss structure with the necessary mounting plates for subsystem hardware; a six-axis vibration isolation system which can support a reaction wheel assembly to provide a flight-like input disturbance source; a complete Michelson interferometer; internal and external metrology systems; and a star simulator that injects the stellar signal into the interferometer collecting apertures. Figure 3 compares the present MPI configuration with the SIM mission concept in terms of toplevel system parameters and requirements.

The primary objectives of the testbed related to vibration attenuation performance are to: (1) demonstrate the 10 nm positional stability requirement in the ambient lab disturbance environment, (2) predict whether the 10 nm positional stability requirement can be achieved in the anticipated on-orbit disturbance environment, and (3) validate integrated modeling tools that will ultimately be used to design the actual space missions. This paper presents , results which represent the latest advancements made on the testbed in these three areas.

The testbed evolution has followed a phased delivery [17]. Each phase is marked by a major configuration change by following a design, procurement, integration and test sequence. The first major delivery was the bare structure in 1991 [18]. The next major delivery was the first interferometer baseline with the six-axis isolation system in 1994 [19]. The final phase will be a two baseline system by the end of 1998. The testbed is presently well into the test phase of the single interferometer configuration. The paper describes this testbed configuration and results from this phase.

2 DISTURBANCE SOURCES

2.1 Ambient Laboratory

This disturbance class includes all sources that affect the interferometer in measurements that will not exist in space. Examples of these sources include building air conditioning, computer cooling fans, gravity, and people walking. Figure 4 shows displacement data, derived from an accelerometer measurement located in the facility which houses the MPI testbed. . The graph maps the disturbance sources to the frequency ranges where known.

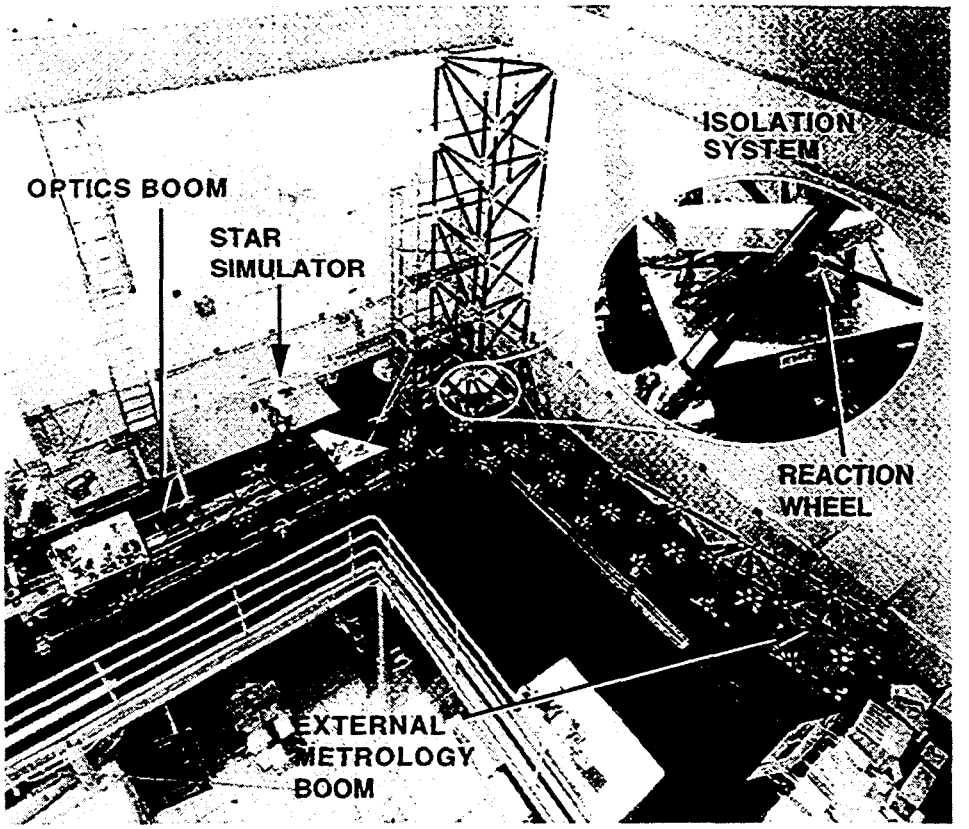

Figure 2: Bird's eye view of the MPI testbed (inset shows close-up of isolator).

The total RMS motion over all frequencies for this measurement is $2300nm$ RMS. Given that this instrument must stabilize optical elements down to the nanometer level, these building disturbances are significant.

These sources manifest themselves as motions of the pseudo star, optical mounts, swaying structure, air turbulence etc. Together these motions from the ambient environment cause RMS motions in optical metrics approximately a factor of 10 higher than what is expected on-orbit. Though the ambient disturbance source is concentrated primarily at low frequency, achieving nanometer positional stabilities in this environment is a challenging problem.

2.2 On-orbit

This class of disturbances includes all sources that are anticipated in the on-orbit environment. The predominant identified source to date are the spacecraft reaction wheel assemblies. Although wheel size is still in question, the SIM design baselines the HST RWA's primarily because these wheels are the quietest wheels flown to date. Fortunately, the HST RWA's have been modeled based on measurements of flight units [20]. In this model, each wheel produces disturbances in five degrees-of-freedom: one axial force (along the wheel spin axis), two radial forces (normal to the spin axis). and two radial torques (wheel wobble). These disturbances result from wheel imbalances and bearing imperfections and are harmonics of

	MICRO-PRECISION INTERFEROMETER TESTBED	SPACE INTERFEROMETRY MISSION
	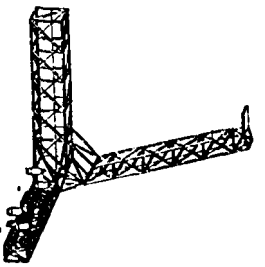	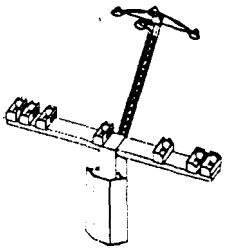
FUNCTIONS	ASTROMETRY	ASTROMETRY & IMAGING
SIZE	7m	10 m
# INTERFEROMETER BASELINES	1 (GUIDE)	(2 GUIDE,: SCIENCE)
RIGID BODY CONTROL	ACTIVE SUSPENSION SYSTEM (1-ARCMIN ACCURACY)	S/C ACS (1-ARCMIN ACCURACY)
STELLAR SOURCES	(SIMULATED) HENE LASER	MAGNITUDE 7 TO 20 (WHITE LIGHT)
DISTURBANCE ENVIRONMENT	1 MAGELLAN FLIGHT SPARE RWA + AMBIENT SEISMIC VIBRATIONS (10 μm (RMS))	4 HST CLASS RWAS (1 μm (RMS))
MASS	400 kg	1728 kg
FRINGE STABILITY	10 nm (RMS)	10 nm (RMS)
COHERENCE TIME (GUIDE)	-1 hr	-1 hr
POINTING STABILITY	0.2 arcsec	0.03 arcsec

Figure 3: Table comparing the SIM mission with the MPI testbed.

the wheel speed with amplitudes proportional to wheel speed squared [20]. As an example, Figure 5 shows the power spectral density of axial force at a wheel speed of 1500 rpm.

3 · CONTROL APPROACH

This section describes the overall vibration attenuation strategy while the instrument is in observing mode. The strategy differs depending on which disturbance rejection problem is being addressed; the ambient lab disturbance or the on-orbit disturbance. Within the context of the layered control strategy depicted in Figure 1, the differences are in optical loop bandwidths and isolation system contribution to the disturbance rejection performance. For the ambient disturbance rejection problem, no limit is given for closed loop bandwidths. Limitations are thus imposed by actuator, sensor or sample rate limitations for example. For the on-orbit disturbance rejection problem, the sensors dictate the closed loop bandwidth based on known limitations on stellar magnitudes anticipated for this mission. This limita-

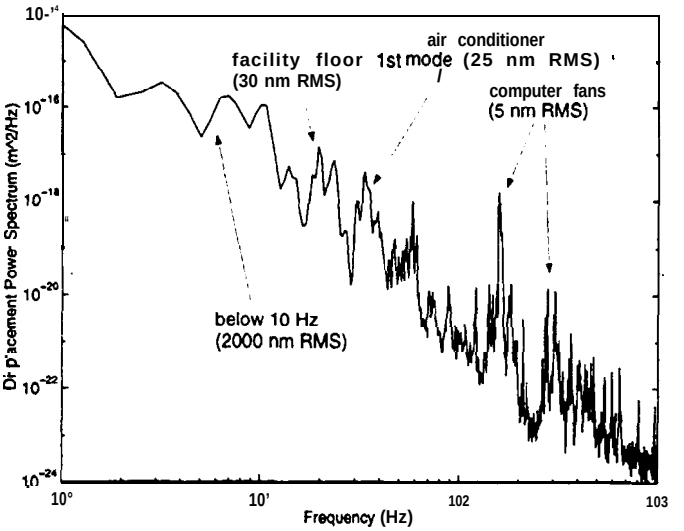

Figure 4: Ambient displacements in the MPI Lab.

tion is set at $300Hz$. The other major difference regards the isolation system. In the ambient disturbance rejection case, this vibration attenuation layer does not participate in improving end-to-end performance since disturbances enter from all directions. This contrasts to the on-orbit case in which the primary disturbance source is the RWA'S which interface to the structure through the isolation system.

Since no model was used to design the MPI testbed, the control strategy was prescribed based on predictions from a previous analysis effort on the FMI [10]. Despite the narrow-band nature of the disturbance, the FMI study provided a broadband disturbance rejection requirement. This study demonstrated the need for broadband disturbance rejection from DC to $1kHz$ of 40-60 dB in order to meet the $10nm$ (RMS) requirement.

As a first cut, the MPI testbed adopted a broadband control strategy to meet these requirements. For the isolation system, this means as soft as possible without interfering with the attitude control system and to accommodate limitations imposed by gravity. For the optics, this means maximum disturbance rejection, from dc to $300Hz$. The function of the MPI testbed is to show how well the RWA disturbance can be rejected given these constraints.

4 SYSTEM DESCRIPTION

Figure 6 shows a system level block diagram of the primary elements that compose the MPI testbed and their relationship to each other. This section discusses each of these elements individually.

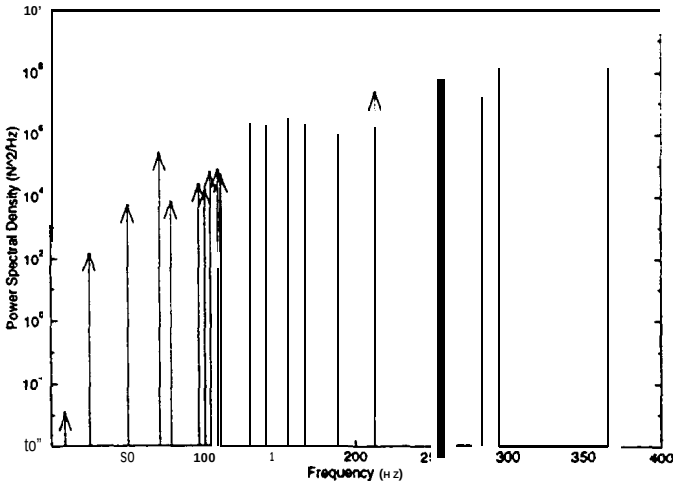

Figure 5: HST reaction wheel axial force disturbance PSD for a wheel spinning at 1500 rpm.

4.1 Structure

The structure is made up of drawn thin walled 6061-T6 aluminum tubes. To correct for "non-straight" tubes, each tube was "floated" in precision end fittings while adhesive was injected and cured [18]. The joint design consists of an aluminum node ball interconnecting two or more struts with "b-nut" interface hardware which allowed simple installation and a mechanism to preload the joints. Details on the structure design and assembly procedures are given in reference [18].

In the initial bare structure configuration, the first flexible mode of the structure was $7.7Hz$ and had an estimated 1 percent modal damping. Initial modal test results showed the bare structure demonstrated extremely linear behaviour [18].

4.2 Suspension System/Attitude Control System.

An active/passive suspension system supports the testbed from the facility ceiling [11]. This system must meet two requirements: (1) isolate the structure from the building, and (2) provide a mechanism to change the rigid body orientation of the structure. Figure 7 shows a close-up view of the device which supports the tower. The device is made up of two systems. A pneumatic system supports the load of the testbed at the particular support location. This is done by supporting the load by an air cushion. The force is defined by the source air pressure and the area of the device's piston. If the air pressure could be regulated precisely, the pneumatic device would be adequate to support the testbed in a desired vertical position. However, the pressure regulators are not ideal. In parallel with this device is a voice coil actuator which provides a centering function to hold the testbed in the desired position. In addition, the voice coil actuator allows for changes to the testbed's rigid body orientation. Four of these devices (three active, one passive) suspend the testbed from the facility ceiling. With this system, all 6 rigid body modes are in the $0.1Hz$ region.

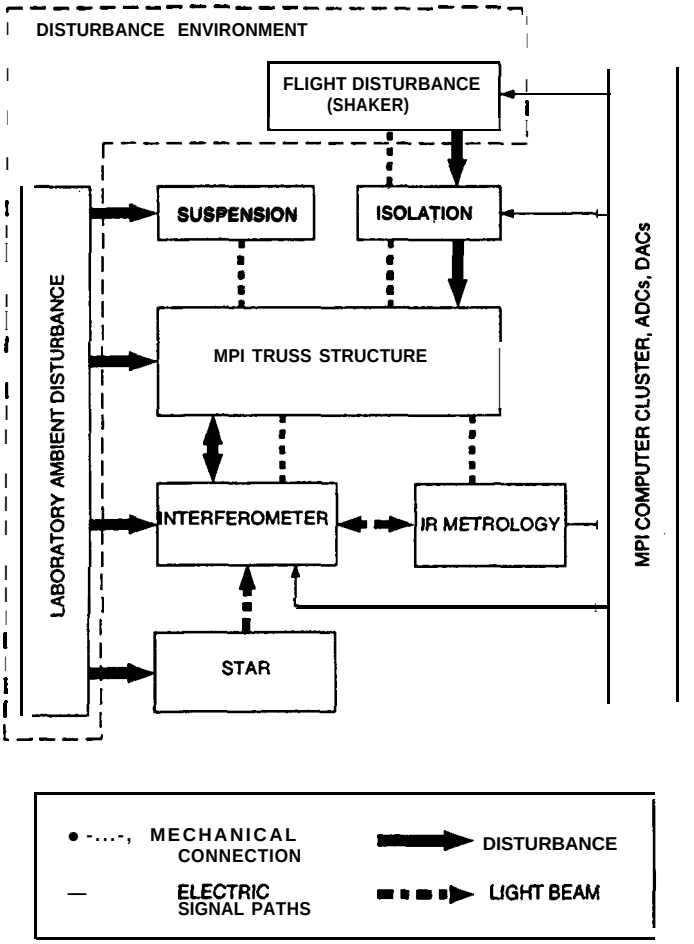

Figure 6: System block diagram showing therelationships between themajor MPI testbed subsystems.

4.3 Artificial Star

Figure 8zoomsin onthetestbed optics boom andtraces thestellar optical path through the artificial star and through the testbed optical train. The included schematic diagram calls out important optical components. In addition, the inset in Figure 8 indicates the changes in the stellar beam cross section at the respective locations in the optical path. The following artificial star and interferometer descriptions trace the stellar optical path through the system.

The "star" source is the laser head of a commercial laser interferometer system that sits on a pneumatically supported optical table. The laser output is a 6 mm diameter beam carrying two orthogonally polarized beams which differ in frequency by 1.8 MHz. The beam is expanded to 30 mm and then split by a polarizing beamsplitter. A number of fold mirrors direct the polarized beams to final fold mirrors located near the corresponding interferometer collecting aperture location. The final fold mirrors, which direct the stellar beam from the table to the MPI structure, are mounted on supports that overhang the suspended structure,

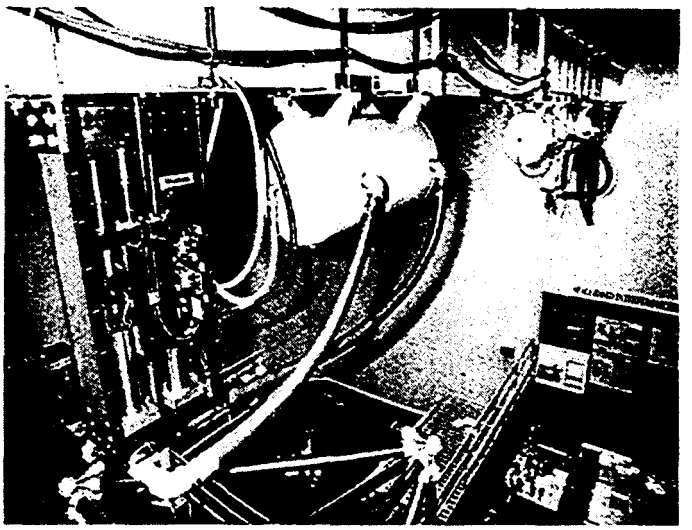

Figure 7: Close-up of the pneumatic/electro-magnetic device which suspends and articulates the MPI testbed.

to provide vertical feed to the siderostats.

4.4 Interferometer

The two interferometer beam paths experience symmetrical reflections in the two interferometer arms on the testbed. The following discussion traces the "inboard" beam path (collecting aperture on the right-hand side of the figure) without loss of generality. The two-axis gimbaled siderostat mirror contains a 12 mm corner-cube retroreflector used by the internal metrology system. Therefore, the beam leaving the siderostat consists of an annular stellar beam and a central infrared metrology beam. A 90/10 beamsplitter picks off 10% of this beam and sends it to a coarse acquisition sensor (a position sensitive device, PSD), used by the siderostat to initially acquire the star. The remaining light travels to the two-axis, high bandwidth steering mirror which sends the light into the active delay line.

The output beam from the active delay line reflects off three fold mirrors, sending the beam to the "outboard" plate (closest to the collecting aperture on the left-hand side of the figure). The third fold mirror. directs the beam from the inboard siderostat to the beam combiner, where it is reflected to join the the transmitted beam from the outboard siderostat. After the beam combiner, the central portion of the combined stellar beams passes through the hole in the annular pick-off mirror to a fringe detector as a single beam with two orthogonally polarized components, with frequencies differing by 1.8 MHz and with a phase difference which depends on the optical path difference for the two arms. The detector, a standard receiver for the commercial interferometer, produces a 1.8 MHz heterodyne signal

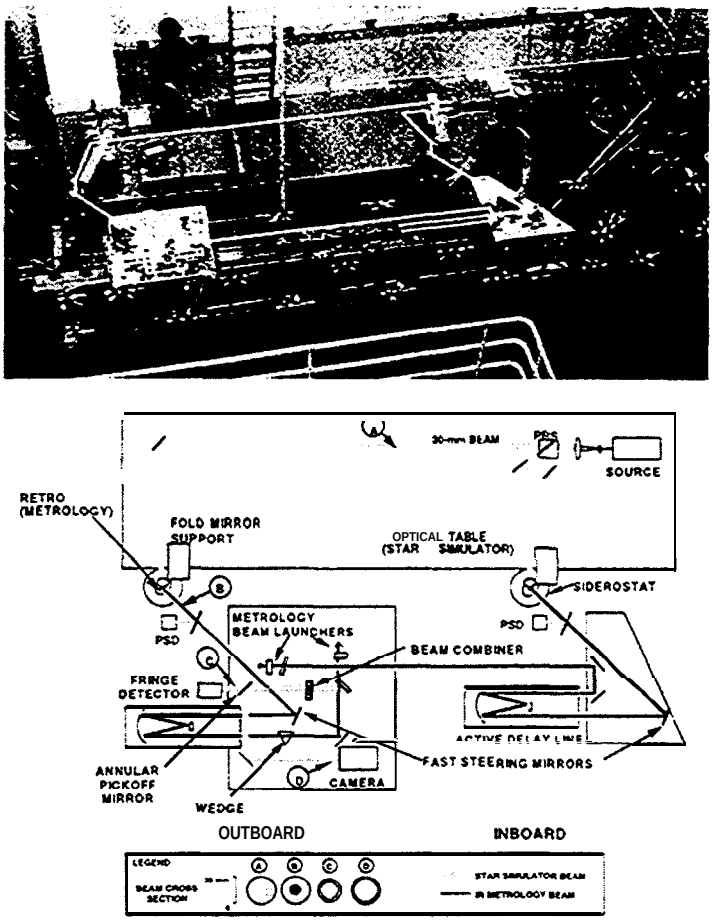

Figure 8: Optical layout for the first MPI baseline from star simulator to optical detectors. The schematic diagram and the photograph depict the same regions of the testbed. The inset shows the beam cross section at different points in the optical path.

with a phase that varies as the fringe position of the stellar beams changes. The annular pick-off mirror reflects the outer portion (30 mm OD and 25 mm ID) of each stellar beam towards a digital CCD camera.

Finally, the outboard optical path contains an additional wedge that has a central hole which corresponds to the pick-off mirror hole diameter. This causes the outer annular region of the beam from the outboard siderostat to be deflected by 1 arc minute while the center portion passes unreflected. Thus, at the pick-off mirror, the central portions of the beams are parallel, while the outer regions propagate along directions making a 1 arc minute angle. The two reflected beams are therefore focused at different points on the CCD camera, which allows to sense the pointing of the two beams with a single sensor. The digital image is processed in real time in order to find the centroid of the beam images. The algorithm currently in use determines the position of the image centroid with a resolution of 0.01 pixels. For additional details on the optical system, see [21].

4.5 Internal Metrology System

In addition to the stellar beams, two independent internal metrology beams trace the internal paths (from beam combiner to corner-cube retroreflectors at thesiderostats) of each interferometer arm. In contrast to the visible stellar beam, the internal infrared metrology system is a two-pass system. The infrared metrology is also based on heterodyne interferometry. Light with λ=1319 nm from a Nd:YAG laser is split into two beams with orthogonal polarizations. Each polarization component is frequency-shifted by using an acousto-optic modulator, for a frequency difference of 2 MHz. The infrared light is fed via fibers to beam launchers in close proximity to the beam combiner, where the metrology beams are injected into the system through holes bored in neighboring fold mirrors (see outboard plate in Figure 8).

4.6 External Metrology System

The external metrology monitors changes in the relative positions of the different interferometer baselines. It does this by launching a large number of metrology beams from the external metrology boom, to each siderostat which contain corner cube retroreflectors in the center. Together, these beams form an optical truss. The external metrology system uses the same Nd:YAG laser system and the same type of beam launchers described" previously. To date, the primary MPI effort has focused on understanding the limitations for performing these measurements in air. This system will become important when the second baseline is added in late 1998.

4.7 Isolation System

Figure 2 shows a close-up of MPI's six-axis vibration isolation system. The top plate provides an interface for actual reaction wheels, rotational shakers or linear translating shakers. The shakers either emulate the reaction wheel disturbance or provide a broadband disturbance input for transfer function measurements. The objective of the isolator is to pass low frequency reaction wheel control torques across the mount while simultaneously preventing the undesirable, high frequency reaction wheel disturbance harmonics from passing across the mount.

The mount design utilizes a passive and active isolation capability. The approach is to enhance the mounts' inherent passive performance with an active stage. The mount consists of 6 identical isolator struts arranged in a mutually orthogonal hexapod configuration. Each strut contains a simple voice coil actuator, a parallel motion flexure that connects the voice coil magnet to the coil (providing the passive stiffness), and a force transducer for feedback. The control strategy is to close six independent S1S0 loops to actively soften each strut's passive stiffness by a factor of 10-100 thereby moving the mount's passive corner frequencies down by a factor of 3-10. The present system has a 10 Hz passive mount corner frequency. For more details on the isolation system, see reference [22].

4.8 Real-Time Computer System

All instrument control functions areprovided byadi@tal real-time computer system. The instrument operator sits at a SUN workstation which is the host to a VME-based system that provides the real-time control functions. These functions range from instrument sequencing through different operating modes to the individual digital controller implementations. The VME system houses 10 cpu's in five separate VME back planes; each dedicated to a specific subsystem. These cardcages are all synchronized to a central clock which provides the interrupt trigger for the system. In addition, each cage contains a reflective memory board which reflects the memory from each subsystem to all the others in the system. This emulates all the cpu's being on the same backplane, when in reality they exist on separate backplanes. This architecture allowed parallel subsystem integration and minimizes backplane bus traffic since all high rate communications are local to a single cage. The Palomar Testbed Interferometer uses this same design. Further details are described in reference [23].

5 MODES OF OPERATION

The primary operating mode of interest on the testbed is when the interferometer "observes" a star. This is the operating mode when the $10nm$ requirement must be demonstrated. However, to reach this condition, as with the on-orbit instrument, requires a large number of initialization, calibration and acquisition procedures. Figure 9 provides a high level sequence of operations that must be executed to reach "observing" mode. All of these sequential operating modes use a subset of the elements described in the System Description section of this paper.

Figure 9: High-level sequence of operating modes to reach instrument "observing" mode.

5.1 Coarse Acquisition System

Figure 10 shows a block diagram of the coarse acquisition system. This system is responsible for placing the two incoming stellar beams on the fine pointing camera located at the end of the optical train. Quasi-static disturbances such as thermal variations in the labor dynamic rigid body motions of the star relative to the swaying testbed cause the wave fronts of the two incoming beams to become non-parallel. The coarse acquisition system rejects these low frequency large amplitude (milliradian) disturbances. The pointing error is sensed with a two-dimensional PSD placed in the focal plane of a lens that focuses the beam which is picked off the main beam by a 90/10% beamsplitter. The PSD null position is co-boresighted with the center of the camera located at the end of the optical train. The PSD output is digitized at $2kHz$ and filtered with a second order low pass with a cross-over frequency of 2Hz. The loops are all decoupled so that the same filter is used for both axes, on both

siderostats. The compensator output is fed to the siderostat controller, which generates the signals that operate the micro-stepper motors controlling the two pointing degrees of freedom of the siderostat.

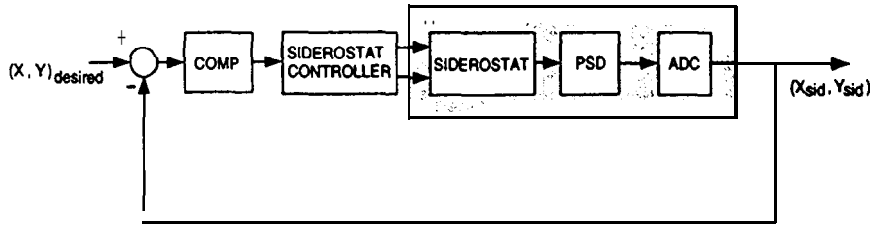

Figure 10: Block diagram of the coarse acquisition system.

5.2 Fine Pointing System

Once the spots from the two interferometer arms are on the camera, the fine pointing system maintains parallel wavefronts in the presence of the higher frequency disturbances. Figure 11 shows a block diagram of the pointing control system. The fast steering mirror has a bandwidth of 1 kHz and an angular range of 70 arcsecs. Three symmetrically oriented piezo actuators position the mirror, providing tip and tilt motion. The sensor for the pointing control subsystem is a high-frame-rate 32 x 32 pixel CCD camera. During closed loop operation, only a 5 x 5 pixel window is transferred from the camera to the processor enabling high sample rates. The dedicated processor for this loop calculates x, y centroid values for this 5 x 5 image at 4 kHz.

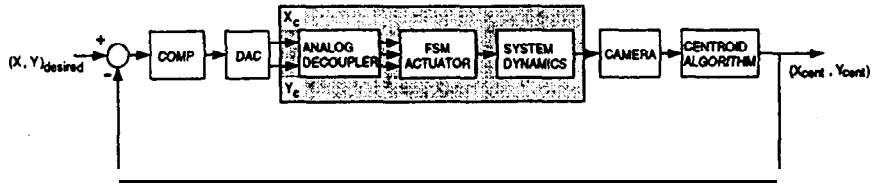

Figure 11: Block diagram of the fine pointing system.

The fundamental approach to the pointing control design is to decouple the x and y tilts resulting in 2 independent single-input, single-output compensators for each interferometer arm. By design, all four of these loops have the same plant transfer function and, therefore, utilize the identical compensator design. The compensator (for all four loops) is 7th order, and provides 60 dB of feedback at low frequency (1 Hz) and the unity gain frequency is $80Hz$. In the presence of the lab ambient noise environment, this control approach stabilizes pointing to 0.27 μrad(RMS) which is a factor of 10 better than the requirement. With the two interferometer arms locked onto the same star, the stellar fringe can now be acquired. See references [19], [24] for more details on the pointing control subsystem.

5.3 Fringe Acquisition

The present HeNe single frequency stellar source does not require acquisition since the fringe position is not unique. The instrument simply selects the fringe position at start-up time as the central fringe position. Once a white light system is installed, this subsystem will be implemented and tested in the ambient and on-orbit vibration environments.

5.4 Fringe Tracking

The purpose of the fringe tracking subsystem is to equalize stellar pathlength from the target star through each arm of the interferometer to the point they are combined.

Figure 12 shows a block diagram of MPI's fringe tracking subsystem.

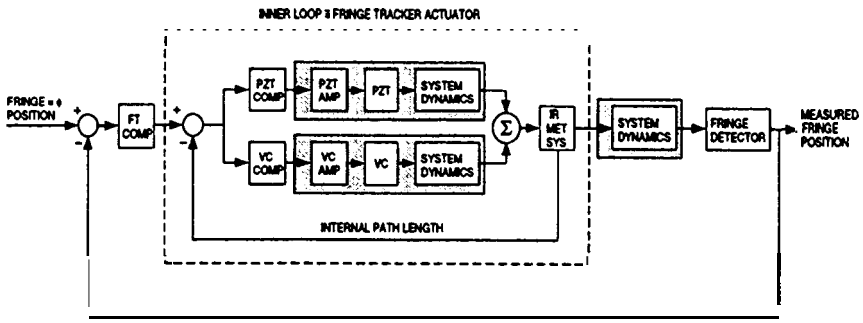

Figure 12: Block diagram of the fringe' tracking system.

The actuator for this subsystem is the active delay line which actually consists of three nested actuators. This three-tiered actuator acts as a linearly translating retroreflector with tremendous dynamic range. A stepper motor provides low frequency (de), long travel capability (m). An intermediate voice coil actuator translates (cm) the entire cat's-eye assembly in the mid-frequency range (dc - 100 Hz). A reactuate piezo supporting the secondary mirror provides the high bandwidth (kHz) precise actuation stage (p-t). The coarse stepper motor is used primarily to slew and acquire a new stellar fringe. Once acquired, this stage is locked down and the other two stages provide the actuation necessary to reject disturbances during an observation.

The MPI fringe detector provides fringe position measurements at 8 kHz. These measurements are subtracted from the desired fringe position (0) to create the error signal to be filtered by the fringe tracker compensator. The bandwidth of the fringe tracking loop is 300 Hz.

The parallel connection of the piezo and voice coil actuators enables rejection of the large amplitude, low frequency disturbances with the large stroke voice coil actuator and the small amplitude , high- frequency disturbances with the piezo actuator. See references [19] and [25] for more details on the fringe tracker control system.

6 MPI INTEGRATED MODEL

The MPI integrated model consists of a structural finite element model and a linear optical model that are integrated together. The structural model is generated with IMOS, whereas both IMOS and COMP [26] are used to create the optical model. The integration and analysis are performed in MATLAB [27] with the aid of IMOS functions.

6.1 Structural Model

The structural model is specified in IMOS as a finite element geometry, shown in Figure 13. This geometry consists of plate, beam, truss, and rigid body elements, modeling the base truss structure and the components. The base truss structure is made up of three booms: the horizontal optics boom, the vertical tower, and the canted metrology boom. The components consist of inboard and outboard optics plates, a disturbance mount plate, two siderostat mounts, an optics cart containing an active delay line, the optics cart support structure, a hexapod isolation system, a passive delay line, and an external metrology beam launcher plate. The finite element model uses 2,577 degrees of freedom (dof) of which 1,832 dofs are independent with respect to the multi-point constraints (MPCs) of the rigid body elements (RBEs) [12].

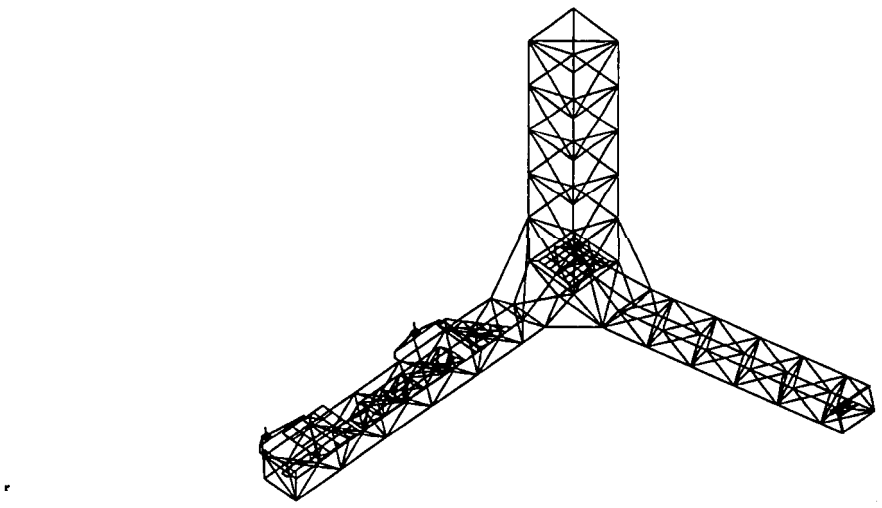

Figure 13: MPI finite element geometry (compare with Figure 2).

The plate and beam properties as well as the finite element geometry itself have been refined by incorporating MPI modal test data into the model. The structural model updating has been done in two phases, following the phased delivery of the MPI testbed. The first phase involved estimating the parameters of the beams comprising the base truss structure from modal testing performed on the bare truss [28, 29]. The second phase involved geometry

modification and parameter estimation of the optics cart support structure, using *in situ* component modal test data [31, 30],

From the finite element geometry and its associated properties the system mass and stiffness matrices are built. The result is a second-order, state-space description of the form:

$$M\ddot{d} + Kd = B_f f \tag{1}$$

where M and K are the system mass and stiffness matrices, d is the nodal state, f is a vector of force input, and B_f is the force influence matrix.

After the system mass and stiffness matrices are built, multi-point constraints are generated using RBE elements. These constraints take the form of [12]:

$$d = \begin{bmatrix} d_n \\ d_m \end{bmatrix} = \begin{bmatrix} I_n \\ G_m \end{bmatrix} d_n = G d_n \tag{2}$$

where d_n are the independent degrees of freedom and d_m are the dependent degrees of freedom. These constraints are then applied to Equation 1, reducing the state of the system to the independent degrees of freedom:

$$\begin{aligned} G^T M G \ddot{d}_n + G^T K G d_n &= G^T B_f f \\ M_{nn}\ddot{d} + K_{nn} d &= B_{nf} \text{ f} \end{aligned} \tag{3}$$

The eigensolution of Equation 3 is found, yielding flexible-body modes and modeshapes. The resultant diagonalized system is:

$$\begin{aligned} \ddot{\eta} + 2Z\Omega\dot{\eta} + \Omega^2\eta &= \Phi_n^T B_{nf} f \\ d &= G\Phi_n \eta \end{aligned} \tag{4}$$

where η is the modal state vector, Z is a diagonal modal damping matrix, Ω is the diagonal modal frequency matrix, and Φ_n is the eigenvector matrix. Z is formed by assuming a modal damping of 0.3% for flexible body modes above 32 Hz and damping ranging from 0.15% to 0.45% for modes below 32 Hz. These damping values correspond to estimates obtained from the second phase of modal tests.

6.2' Optical Model

The optical model begins with a specification of the optical prescription. This prescription includes the shapes, positions, and orientations of the optical elements. A ray trace of the optical prescription is shown in Figure 14. This optical prescription is generated in IMOS based on the prescription of the actual optical elements of MPI. The model generation uses the structural finite element geometry in order to simplify the prescription definition and to ease the succeeding structural-optical model integration. This allows the location of the actual optical elements to be measured with respect to reference points on the structure as opposed to with each other. Furthermore, structural nodes that correspond to optical element 'attachment points are easily identified or defined.

Once the optical prescriptions are specified, they are exported to COMP, where linear optical models are created. These linear models are calculated by performing an analytic differential ray trace [26]. The result is a model of the form:

$$y = C_{opt} d \tag{5}$$

where u! is a vector of optical element position and orientation perturbations, y is a vector of optical output, and C_{opt} is the optical sensitivity matrix. The optical output can be pathlength, wavefront tilt, or spot motion.

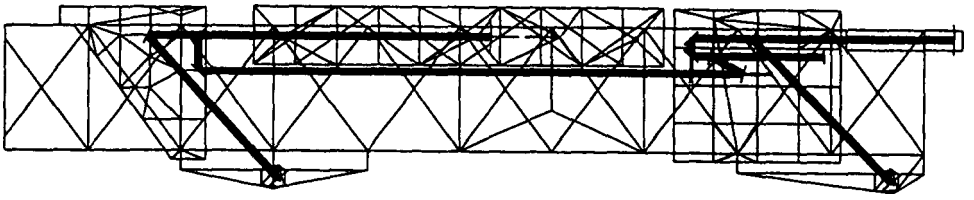

Figure 14: Ray trace of the MPI optical prescription on the finite element geometry of the optics boom.

6.3 Structural-Optical Model Integration

Once the structural modal model and the linear optical model have been created, they are integrated to form a structural-optical model. This integrated model is specified in first-order, state-space from, lending itself most easily to analysis with existing MATLAB functions. In particular, the state-space integrated model can be used for frequency-domain analysis, time-domain simulation, and closed-loop synthesis.

First, the structural model is truncated to remove modes above the bandwidth of expected disturbances (*i.* e., above 900 Hz) [15, 13]. The truncated modal model is then converted into first-order, state-space form by using the substitution [12]:

$$x = \begin{bmatrix} \eta_k \\ \dot{\eta}_k \end{bmatrix} \tag{6}$$

Resulting in:

$$\begin{aligned} \dot{x} &= Ax + Bu \\ d &= C_d x + Du \end{aligned} \tag{7}$$

with:

$$\begin{aligned} A &= \begin{bmatrix} 0 & I \\ -2Z_k\Omega_k & -\Omega_k^2 \end{bmatrix} \quad B = \begin{bmatrix} 0 \\ \Phi_{nk}^T G^T B_f \end{bmatrix} \\ C_d &= \begin{bmatrix} G\Phi_{nk} & O \\ O & G\Phi_{nk} \end{bmatrix} \qquad D = O \end{aligned} \tag{8}$$

where the subscript k refers to the set of kept modeshapes.

Finally, the linear optical model is incorporated into the first-order model. The optical output is obtained by premultiplying d by the optical sensitivity matrix, C_{opt}. In this case the matrix C of the measurement equation of Equation 7 becomes:

$$C = C_{opt} C_d \tag{9}$$

Note that the matrix D of Equation 7 is still zero but now has different dimension.

7 RESULTS

7.1 Ambient Performance Measurement

Figure 15 shows a step response of the fringe tracker system in the ambient MPI lab disturbance environment. The predominant recognizable disturbance when the loop is open is the one Hz flexure mode of the active delay line. This is likely due to motion of the entire structure which in turn excites the delay line flexure mode. Air turbulence and fluctuations in the air pressure which in turn perturbs the suspension system set point are the sources of these disturbances. Over all frequencies, the fringe position is 1930 nm RMS during this run while the loop is open. With the loop closed, the fringe position jitter is reduced to 8.1 nm RMS. The majority of the energy in this closed loop fringe position is around 100 Hz and is from the computer cooling fans.

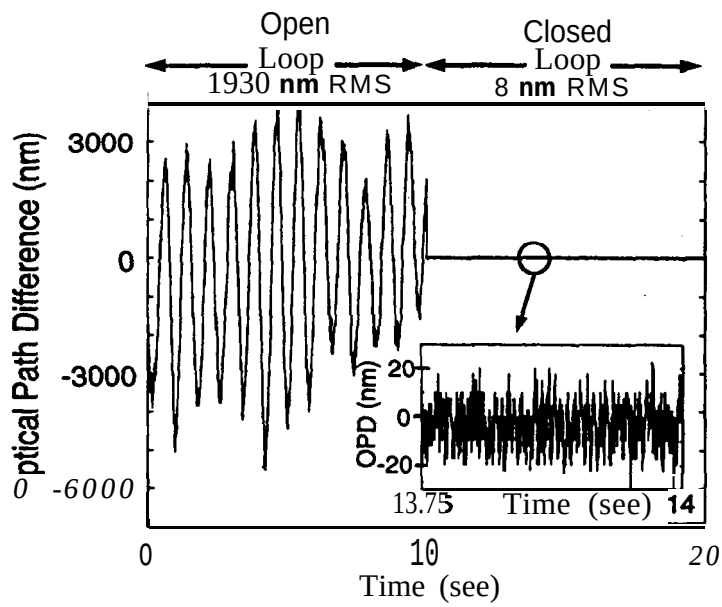

Figure 15: Optical path difference as a function of time for the fringe tracker loop open and closed.

7.2 On-Orbit Performance Prediction

This section presents results showing how the present MPI control design would perform in the on-orbit disturbance environment. The approach to measure on-orbit performance in a ground-based lab setting uses disturbance transfer functions acquired from the MPI testbed combined with an analytical disturbance model of the RWA'S. This novel performance prediction algorithm predicts instrument performance in an accurate, efficient way, covering the entire range of possible RWA disturbance conditions that would occur during an instrument observation [32]. The effectiveness of the layered control technology can be evaluated by predicting instrument performance in three configurations. These configurations are: the no control condition (hard mounted disturbance, no active optics); active optics (hard mounted disturbance, optical control loops operational); and the completely active condition (active isolation of disturbance, optical control loops operational). The six transfer functions (3 forces, 3 torques) from the shaker input mounting location to fringe position output, were measured for each of these configurations. Figure 16 shows an example for one direction (x-axis torque), in two different instrument configurations: (1) the no control condition, and (2) the completely active condition. Comparison of these two plots indicate the broadband nature of the layered architecture in which the active optics provides vibration attenuation at low frequencies and the active/passive isolation system provides vibration attenuation at high frequencies. Reference [19] discusses in more detail the distribution of labor between the different vibration attenuation layers.

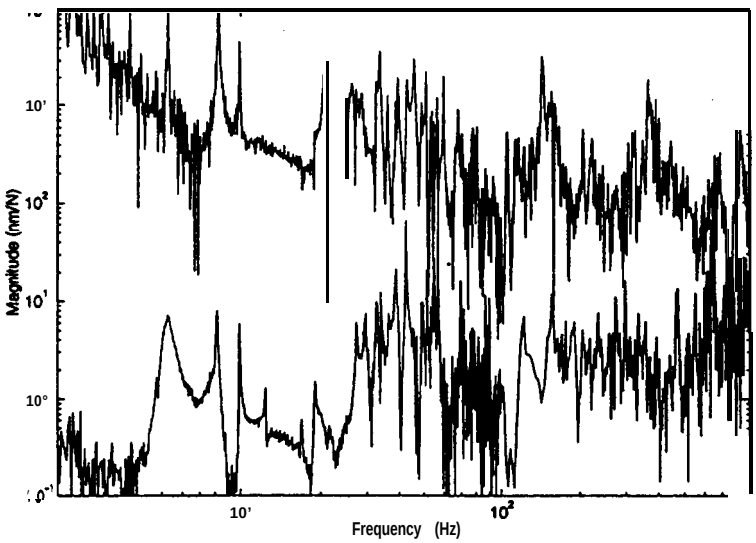

Figure 16: Disturbance transfer functions in the x torque direction for the no control (upper curve) and completely active conditions (lower curve).

An example of the parameterized result from this performance prediction algorithm is given in Figure 17. This figure displays the fringe position variation as a function of wheel speed for a single wheel for the three control configurations. There is one plot for each of the four reaction wheels.

Norms defined to summarize these parameterized fringe position variation functions into a single number are defined in reference [32]. Table 1 summarizes results from a four wheel system in all different control configurations [32]. Note that for the completely active condition, considering all four wheels, the predicted RMS fringe position is 10.1 nm.

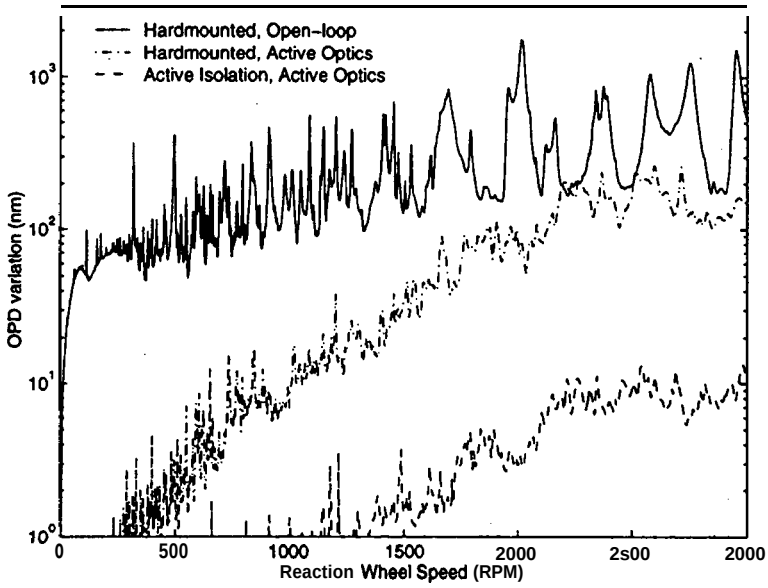

Figure 17: Predicted on-orbit fringe position variation as a function wheel speed for a single wheel.

7.3 IMOS Model Validation

The disturbance transfer function is the primary function used to validate the IMOS model. Measured transfer functions from the testbed are compared with the same predicted transfer functions from the model. Figure 18 compares a measured and predicted transfer function for the x-axis force direction. The value of a broadband metric is given in the legend for each transfer function. The predicted transfer functions for this open loop configuration are within a factor of two of the measured transfer functions [33].

8 CONCLUSIONS

This paper presents the latest results from all MPI activities that address vibration attenuation issues for spaceborne optical interferometers. Present fringe position stabilization in the ambient lab disturbance environment is better than the required on-orbit performance. To further improve upon the 8.1 nm RMS will likely require controlling the environment. Present efforts are focused on isolating the optical paths from air turbulence, isolating the computer cooling fans, etc. All of these activities will improve the present single baseline

Wheel Number	Disturbance Hardmount No Control		Disturbance Hardmount Active Optics		Active Isolation Active Optics	
	σ_{rms}	σ_{max}	σ_{rms}	σ_{max}	σ_{rms}	σ_{max}
1	398.2	1764	94.2	266.2	4.9	13.4
2	375.4	1773	93.3	254.1	4.9	13.4
3	380.5	1498	92.9	246.9	5.2	15.8
4	311.4	1465	89.5	235.5	5.2	14.7
All	735.7	3263	185.0	501.8	10.1	28.7

Table 1: Predicted on-orbit fringe position (in nanometers) for three controller configurations. Each configuration contains two metrics: σ_{rms} - RMS fringe position variation over wheel speed, and σ_{max} - maximum fringe position variation over wheel speed.

performance, but will play a larger role in the two baseline configuration which is the next and final phase of the testbed.

The on-orbit predicted performance needs to be improved for the worst case operating conditions $(28nmRMS)$. Three areas are underway to address this need: (1) apply the structural quieting layer to improve performance, (2) improve the transfer function measurement approaches used, particularly torque measurements, and (3) apply narrowband active isolation algorithms to chase the RWA harmonics as they migrate over wheel speed variations.

Finally, ongoing activities in the modeling area include validation of the methodology for various closed-loop configurations [34] and assessing the sensitivity of these results to the accuracy of the structural model [35].

References

[1] Solar System Exploration Division, TOPS: Towards Other Planetary Systems, National Aeronautics and Space Administration, Washington, D. C., 1992.

[2] M.M. Colavita, M. Shao, M.D. Rayman, "0S1: Orbiting Stellar Interferometer for Astrometry and , Imaging," Applied Optics, Special Section on the Williamsburg Space Optics Conference, 1991.

[3] M. Shao, "Orbiting Stellar Interferometer: Proceedings of the SPIE Symposium on OE/Aerospace, Science and Sensing, Conference on Spaceborne Interferometry, vol. 1947, pp. 89, Orlando, FL, April 1993.

[4] M. Shao and D. M. Wolf, "Orbiting Stellar Interferometer," Proceedings of the SPIE Symposium on OE/Aerospace, Science and Sensing, Conference on Spaceborne Interferometry, vol. 2447, pp. 228-239, Orlando, FL, April 1995.

[5] M. Shao, M.M. Colavita, B.E. Hines, D.H. Staelin, D.J. Hutter, K.J. Johnston, D. Mozurkewich, R.S. Simon, J.L. Hersey, J.A. Hughes, and G.H. Kaplan, "Mark 111 Stellar Interferometer," Astron. Astrophys. 193,357-371 (1988).

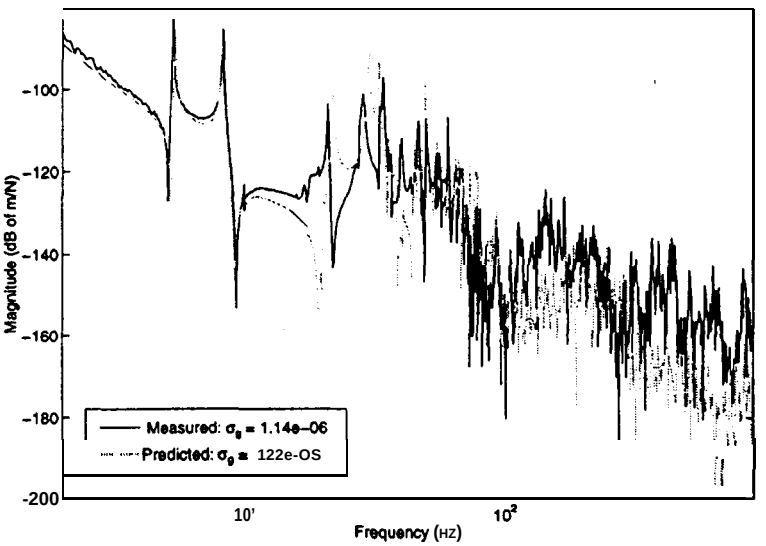

Figure 18: Comparison of measured and predicted transfer functions for the x-axis force direction.

[6] M.M. Colavita, M. Shao, B.E. Hines, J.K. Wallace, Y. Gursel, C.A. Beichman, X.P. Pan, T. Nakajima, and S.R. Kulkarni, "Palomar Interferometer Testbed," S.R. 1994, Proceedings SPIE, 2200,89-97.

[7] R. A. Laskin, "Technology for Space Optical Interferometry", Proceedings from the 33rd Aerospace Sciences Meeting and Exhibit, AIAA vol 95-0825, Reno, NV, January 1995.

[8] Y. Gursel, "Laser Metrology Gauges of 0S1," Proceedings of the SPIE Symposium on OE/Aerospace, Science and Sensing, Conference on Spaceborne Interferometry, vol. 1947, pp. 188-197, Orlando, FL, April, 1993.

[9] Y. Gursel, "Metrology for Spatial I.nterferometry," Proceedings of the SPIE Symposium on OE/Aerospace, Science and Sensing, Conference on Spaceborne Interferometry, vol. 2447, pp. 240-258, Orlando, FL, April, 1995.

[10] R.A. Laskin and M. San Martin,''Control Structure System Design of a Spaceborne Optical Interferometer," Proceedings of the AAS/AIAA Astrodynamics Specialist Conference, Stowe, VT, 1989.

[11] D.A. Kienholz, "Defying Gravity with Active Test Article Suspension System," Journal of Sound and Vibration, April 1994, pp. 1420.

[12] M. Milman, *et al.*, "Integrated Modeling of Optical Systems User's Manual, Release 2.0," JPL D-13040, November 15, 1995.

[13] S. Shaklan, J. Yu, and H.C. Briggs,''Integrated Structural and Optical Modeling of the Orbiting Stellar Interferometer," SPIE Space Astronomical Telescope and Instrument II Conference, Orlando, FL, April, 1993.

[14] J.W. Melody, "SONATA Integrated Model and Open LQOP Disturbance Analysis," JPL 10M 3411-95-235csi, June 26, 1995.

[15] J.W. Melody and H.C. Briggs, "Analysis of Structural and Optical Interactions of the Precision Optical Interferometer in Space (POINTS)," Proceedings of the SPIE Symposium on OE/Aerospace, Science and Sensing, Conference on Spaceborne Inteferometry, vol. 1947, pp. 4457, Orlando, FL, April, 1993.

[16] J.T. Spanos, Z. Rahman, C. Chu, and J.F. O'Brien, "Control Structure Interaction in Long Baseline Space Interferometers," 12th IFAC Symposium on Automatic Control in Aerospace, Ottobrunn, Germany, September 7-11, 1992.

[17] G. W. Neat, L. F. Sword, B. E. Hines, and R. J. Calvet, "Micro-Precision Interferometer Testbed: End-to-End System Integration of Control Structure Interaction Technologies; Proceedings of the SPIE Symposium on OE/Aerospace, Science and Sensing, Conference on Spaceborne Interferometry, vol. 1947, pp 91-103, Orlando, FL, April 1993.

[18] L.F. Sword and T.G. Carrie, "Precision Truss Structures from Concept to Hardware Reality: Application to the Micro-Precision Interferometer Testbed," Proceedings of the SPIE Symposium on OE/Aerospace, Science and Sensing, Conference on Spaceborne Interferometry, vol. 1947, pp 104-113, Orlando, FL, April 1993.

[19] G. W. Neat, J. F. O'Brien, N. M. Nerheim, R. J. Calvet, H. Singh, and S. Shaklan, "Micro-Precision Interferometer Testbed: First Stabilized Stellar Fringes," Proceedings of the SPIE International Symposium on AeroSense, Conference on Spaceborne Interferometry II, vol. 2477, pp. 104115, Orlando, FL, April 1995.

[20] M.D. Hasha, "Reaction Wheel Mechanical Noise Variations: LMSC EM SSS 218, June 1986.

[21] B. E. Hines, "Optical Design Issues for the Micro-Precision Interferometer Testbed for Space-Based Interferometry," Proceedings of the SPIE Symposium on OE/Aerospace, Science and Sensing, Conference on Spaceborne Interferometry, vol. 1947, pp. 114125, Orlando, FL, April 1995.

[22] J.T. Spanos, Z. Rahman, and G. Blackwood, "A Soft 6-Axis Active Vibration Isolator," Proceedings of the American Control Conference, pp. 412-416, Seattle, WA, June, 1995.

[23] B.E. Hines, "ASEPS-0 Testbed Interferometer Control System," Proceedings SPIE Amplitude and Intensity Spatial Interferometry II 2200, pp. 98-109, 1994.

[24] J.F. O'Brien and G. W. Neat, "MicroPrecision Interferometer: Pointing Control System," Proceedings of the 4th Conference on Control Applications," Albany, NY, September, 1995.

[25] G.W. Neat and J.F. O'Brien, "Micro-Precision Interferometer: Fringe Tracker Control System," Proceedings of the 19th Annual AAS Guidance and Control Conference, AAS-96-064, Breckenridge, CO, February, 1996

[26] D. Redding, "Controlled Optics Modelling Package User Manual, Release 1.0," JPL D-9816, June 1, 1992.

[27] "Matlab User's Guide," The Math Works Inc., August 1992.

[28] T. G. Carrie, R. L. Mayes, M. B. Levine-West, "A Modal Test of a Space-Truss for Structural Parameter Identification," Proceedings of the 11^{th} IMAC, Kissimmee, FL, February 1993.

[29] J. R. Red-Horse, E. L. Marek, M. B. Levine-West, "System Identification of the JPL Micro-Precision Interferometer Truss: Test-Analysis Reconciliation," Proceedings of the 34^{th} SDM, La Jolla, CA, April 1993.

[30] J. W. Melody, M. B. Levine-West, "High Fidelity Modeling of Evolutionary Structures in IMOS," Proceedings of the First World Conference on Structural Control, pp WP1-98 - WP1-107, Los Angeles, CA, August 1994.

[31] M.B. Levine-West and J.W. Melody, "Model Updating of Evolutionary Structures," Proceedings of the 15th ASME Biennial Conference on Mechanical Vibration and Noise, Boston, MA, September, 1995.

[32] G.W. Neat and J.W. Melody, "Hybrid Experimental/Analytical Performance Assessment Method to Establish Control Technology Readiness for Spaceborne Interferometry," Submitted to the IEEE Transactions on Control System Technology.

[33] J.W. Melody and G.W. Neat, "Integrated Modeling Methodology Validation Using the Micro-Precision Interferometer Testbed," Proceedings of the 1996 Conference on Decision and Control, Kobe, Japan, December, 1996.

[34] J.W. Melody and G.W. Neat,''Integrated Modeling Methodology Validation Using the Micro-Precision Interferometer Testbed: Closed Loop Results," To be presented at the 1997 American Control Conference, Albuquerque, NM, June, 1997.

[35] S. Joshi, J.W. Melody, and G.W. Neat,''Benefits of Model Updating:A Case Study Using the Micro-Precision Interferometer Testbed," Submitted to the 16th Bi-Annual Mechanical Vibration and Noise Conference: Symposium on Model Updating.